

MATERIALS AND METHODS

A total of 12 short cores were collected in Lake Singkarak during a field campaign in 2017. The core locations were selected using high-resolution reflection-seismic profiles (pinger), which were also used for the construction of a bathymetric map of the lake (Wils et al., 2021). Wils et al. (2021) provide a detailed sedimentological study of each of these cores using multi-sensor core logging (magnetic susceptibility, gamma density and color spectrophotometry), X-ray computed tomography (CT), smear slides, grain size and X-ray fluorescence, augmented by a statistical approach to discern sediment types. These analyses showed that most of them contain a turbidite that could be related to the 2007 Singkarak doublet earthquake based on basin-wide correlation, seismic profiles and a ^{210}Pb -derived age-depth model. The authors identified two coarse-grained subdivisions within this turbidite at two distal core sites, potentially related to the individual earthquakes in the doublet. These distal cores, as well as two slope-proximal cores for methodological verification, were selected for further analysis (Table S1).

Table S1: Core locations

Core Name	Longitude	Latitude
SN17-02B	100°30.0315' E	0°34.5988' S
SN17-04A	100°30.7858' E	0°34.2057' S
SN17-06A	100°31.3882' E	0°33.8693' S
SN17-09A	100°31.0927' E	0°34.9520' S

We characterized the 2007 Singkarak seismo-turbidite in these four sediment cores by grain-size analysis using a Malvern Mastersizer 3000 (Table S2). The complete thickness of the 2007 turbidite in each of the four cores was sampled at 5 mm resolution, increased to 2 mm for the coarse-grained pulses in core SN17-09A. Organic matter, calcium carbonate and biogenic silica were removed from the samples following the procedure described by Van Daele et al. (2016). The GRADISTAT package was used to calculate the geometric mean and sorting values (Blott and Pye, 2001).

The magnetic mineral content is determined by two successive thermomagnetic cycles on a sediment mixture from all four cores (Table S3). During the first heating, magnetization is entirely removed at $\sim 580^\circ\text{C}$ (Figure S3), indicating that the dominant magnetic mineral is low Ti-content magnetite (Dunlop and Özdemir, 2015). The first cooling results in a higher magnetization at room temperature, which is likely due to the transformation of titanomagnetite into pure magnetite during heating (cfr. Dunlop and Özdemir, 1997). In the second cycle, the heating curve is reversible, showing that the transition from titanomagnetite to pure magnetite is stable. Alternatively, a combination of pure magnetite and pyrite—commonly identified in the lake, Wils et al. (2021)—can also explain the observed difference between the first heating and cooling as pyrite may also be transformed into magnetite upon heating (Wang et al., 2008). However, because pyrite is paramagnetic at room temperature, it does not contribute to the remanent magnetization we measured. This indicates that the main magnetic mineral carrying the magnetization in Lake Singkarak is low-Ti content magnetite.

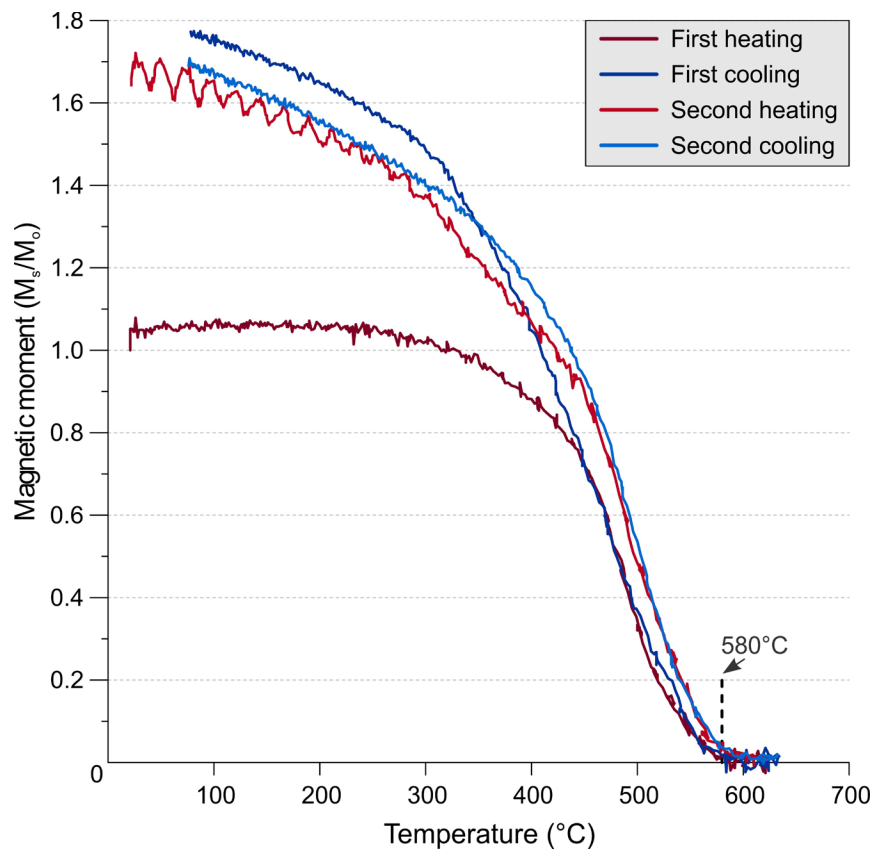


Figure S1: Thermomagnetic curves showing the magnetization behavior during two thermal cycles on a sediment mixture from all four cores. All magnetization is lost above 580°C and returns to higher levels of magnetization compared to the original state after cooling. The second heating and cooling curves are reversible and comparable to the first cooling curve.

To analyze flow directions, U-channel subsamples with a two by two cm cross-section were taken over the full length of each core. To obtain the direction of the paleomagnetic field recorded by these samples, the U-channels were stepwise demagnetized using alternating fields from 0 to 90 mT (18 steps). The magnetization was measured using a 2G 755 magnetometer equipped with high resolution pick-up coils and placed in the mu-metal shielded room of the Laboratoire des Sciences du Climat et de l'Environnement (LSCE) in France. The three degaussing coils were in line with the magnetometer. The direction of the characteristic remanent magnetization (ChRM, i.e. inclination and declination) was defined by principal component analysis with maximum angular deviations (MAD) generally below 3° based on 5 to 17 steps (Table S4), indicating that the magnetization components are mostly well-defined. The magnetic moment of minerals deposited by hemipelagic settling (e.g. background sedimentation) is lined up according to the prevailing magnetic field. Because the time interval covered by the cores is very short, secular variations in the geomagnetic field are not averaged out and we referred to the IGRF model to determine which direction should be observed. In 2007, the declination and inclination at Lake Singkarak were about 0° and -18°, respectively (Thébault et al., 2015). The obtained ChRM is consistent with the expected inclination (Table S4), indicating that the sediments in all four cores reliably record the local geomagnetic field. By aligning the declination of the ChRM, obtained in the reference system of the U-channels, to the magnetic north (0°), we could thus orient the cores in the horizontal plane.

The coarse-grained base of the 2007 turbidite in each of the U-channels were μ CT scanned using the HECTOR μ CT system (Masschaele et al., 2013) of the Ghent University Centre for Tomography (UGCT). The microfocus X-ray source operated at a target voltage of 180 keV and a power of 10 W, with an aluminum filter of 1 mm thick placed in front of the source. All scans were subsequently reconstructed into 3D digital volumes by the specialized reconstruction software Octopus Reconstruction (Vlassenbroeck et al., 2007; Brabant et al., 2011). When the coarse-grained layer of the

turbidite was thicker than 2 cm, stacked μ CT scans were taken to image the required sample length. These were then merged digitally into a single volume using Aquila software (Tescan XRE). A voxel size of 15 μ m was chosen for all overview scans, allowing grains to be visualized down to a size of \sim 100 μ m. Region-of-interest (ROI) scans of the U-channel's center were obtained using a voxel size of 7 μ m, which further improved image resolution. VGStudio ($\text{\textcircled{C}}$ Volume Graphics, version 3.3.1) was used to visualize the μ CT scans.

To digitally identify and measure individual grains, the obtained μ CT volumes were processed using the Avizo software package ($\text{\textcircled{C}}$ Thermo Fisher Scientific, version 2019.4, Figure S1). For consistency, all 3D volumes were processed using the same workflow. As distortion along the sides of the U-channel during retrieval is rare but cannot be ruled out, sub-volumes were extracted to retain only the core of the U-channel (Figure S1A). A radiodensity threshold was subsequently applied so that low-density material was excluded. The remaining high-density material was mostly related to grains, occasionally showing artificial small holes due to a locally lower radiodensity within a single grain (Figure S1B). To avoid erroneous segmentation later on, these holes were digitally filled in (Figure S1C). All resulting digital objects were subsequently eroded and dilated (i.e. binary opening operation) to remove the smallest objects without altering the shape and size of larger objects (Figure S1D). This was done by subtracting and adding 1 pixel to all objects in the overview scans, but increased to 2 pixels for the ROI scans due to their higher resolution and thus the more numerous presence of smaller objects that impeded the subsequent segmentation of the larger objects into individual grains. Finally, a watershed algorithm was applied to separate all objects into numerous digital grains (Figure S1E). Each individual grain was labelled (Figure S1F) and analyzed for its elongation and orientation (trend and plunge, Figure S2). Parts of the turbidite that were not adequately segmented by this procedure were not further considered.

SN17-06A processing steps

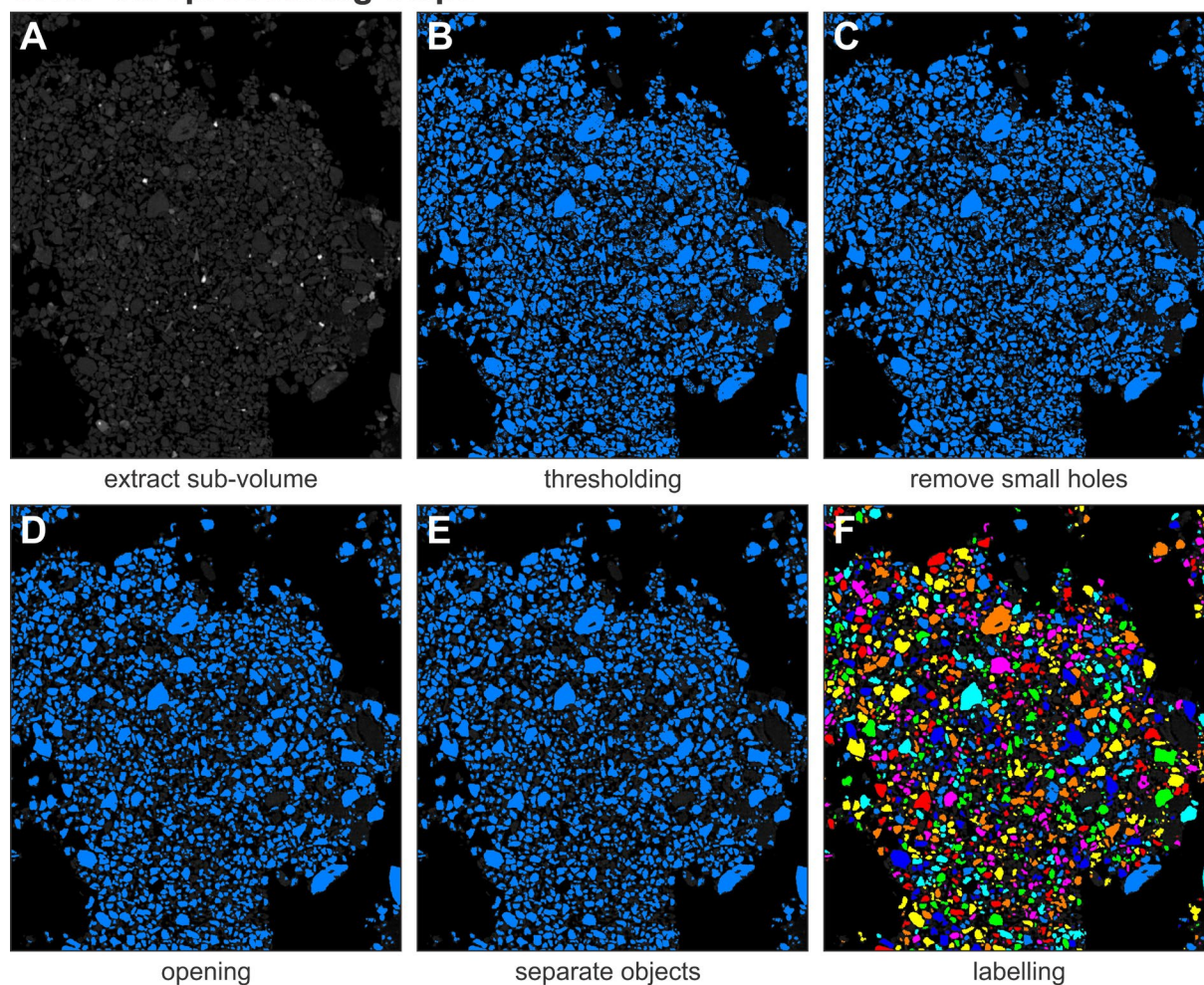
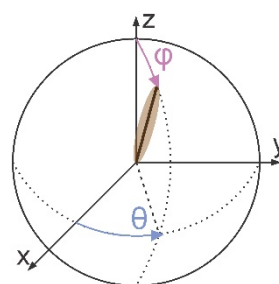


Figure S2. Visualization of a single, 2D-slice of core SN17-06A showing stepwise application of the different processing steps (A to F) that have been applied to each 3D μ CT scan using the Avizo software package.



Trend: θ (0-360°)

Plunge: $\phi-90^\circ$ (-90-0°)

Figure S3: Schematic representation of orientation data (θ and ϕ , measured in updip direction) obtained by μ CT analysis, where θ equals the grain trend (ranging from 0° to 360°). For correct representation of all grains by a

stereoplot (where plunge is measured in downdip direction and with respect to a horizontal plane), ϕ -values are corrected by subtracting 90° so that the resulting plunge values range between -90° and 0° .

Only the orientation of grains with equivalent diameters (i.e. diameter of a spherical particle with the same volume) $>100 \mu\text{m}$ were considered as the current μCT data resolution does not allow for adequate digital identification of smaller grains. Moreover, only strongly elongated grains (<0.2 , where 0 is perfectly elongated and 1 is spherical) were included (Table S5). The orientation of the retained grains was subsequently plotted in a stereoplot (Stereonet v.11, Allmendinger et al. (2012); Cardozo and Allmendinger (2013)). This allowed several turbidite pulses (a, b, c, d), marked by a single flow direction, to be identified within each of the coarse-grained intervals (1, 2) of the turbidite. For each of these pulses, the grain-size limit was raised to $150 \mu\text{m}$ to further reduce potential noise in the dataset in case plenty of larger grains (arbitrarily chosen as more than 500) were present. The Bingham axial distribution algorithm (Fisher et al., 1987) was subsequently applied to all remaining grains in a single turbidite pulse to show the principal component and thus objectively reveal the main paleocurrent direction (PC1, Table S6). In case the basal plane of the considered pulse was tilted, likely due to core deformation during or after core retrieval, orientation parameters were corrected so that they are measured with respect to the actual basal plane rather than a horizontal one (Table S5). For thick pulses, this may have resulted in overcorrection for the upper part of the pulse due to gradual flattening of the deposit and hence, an apparent opposite plunge direction for the affected grains.

Note that ChRM and μCT analysis results (declination and trend, respectively) each have their own reference frame with respect to the U-channel (Figure 2, Figure 4).

REFERENCES CITED

- Allmendinger, R. W., Cardozo, N., and Fisher, D. M., 2012, Structural Geology Algorithms: Vectors and Tensors: New York, Cambridge University Press, 289 p.
- Blott, S. J., and Pye, K., 2001, GRADISTAT: a grain size distribution and statistics package for the analysis of unconsolidated sediments: Earth Surface Processes and Landforms, v. 26, p. 1237-1248, <https://doi.org/10.1002/esp.261>.

- Brabant, L., Vlassenbroeck, J., De Witte, Y., Cnudde, V., Boone, M. N., Dewanckele, J., and Van Hoorebeke, L., 2011, Three-dimensional analysis of high-resolution X-ray computed tomography data with Morpho+: Microscopy and Microanalysis, v. 17, p. 252-263, <https://doi.org/10.1017/S1431927610094389>.
- Cardozo, N., and Allmendinger, R. W., 2013, Spherical projections with OSXStereonet: Computers & Geosciences, v. 51, p. 193-205, <https://doi.org/10.1016/j.cageo.2012.07.021>.
- Dunlop, D. J., and Özdemir, Ö., 1997, Rock Magnetism: Fundamentals and Frontiers: New York, Cambridge University Press, 573 p.
- Dunlop, D. J., and Özdemir, Ö., 2015, Magnetizations in rocks and minerals, *in* Schubert, G., ed., Treatise on Geophysics (Second Edition): Oxford, Elsevier, p. 255-308.
- Fisher, N. I., Lewis, T., and Embleton, B. J. J., 1987, Statistical Analysis of Spherical Data: Cambridge, Cambridge University Press, 329 p.
- Masschaele, B., Dierick, M., Loo, D. V., Boone, M. N., Brabant, L., Pauwels, E., Cnudde, V., and Hoorebeke, L. V., 2013, HECTOR: A 240kV micro-CT setup optimized for research: Journal of Physics: Conference Series, v. 463, p. 012012, <https://doi.org/10.1088/1742-6596/463/1/012012>.
- Thébault, E., Finlay, C. C., Beggan, C. D., Alken, P., Aubert, J., Barrois, O., Bertrand, F., Bondar, T., Boness, A., Brocco, L., Canet, E., Chambodut, A., Chulliat, A., Coïsson, P., Civet, F., Du, A., Fournier, A., Fratter, I., Gillet, N., Hamilton, B., Hamoudi, M., Hulot, G., Jager, T., Korte, M., Kuang, W., Lalanne, X., Langlais, B., Léger, J.-M., Lesur, V., Lowes, F. J., Macmillan, S., Mandea, M., Manoj, C., Maus, S., Olsen, N., Petrov, V., Ridley, V., Rother, M., Sabaka, T. J., Saturnino, D., Schachtschneider, R., Sirol, O., Tangborn, A., Thomson, A., Tøffner-Clausen, L., Vigneron, P., Wardinski, I., and Zvereva, T., 2015, International Geomagnetic Reference Field: the 12th generation: Earth, Planets and Space, v. 67, <https://doi.org/10.1186/s40623-015-0228-9>.
- Van Daele, M., Bertrand, S., Meyer, I., Moernaut, J., Vandoorne, W., Siani, G., Tanghe, N., Ghazoui, Z., Pino, M., Urrutia, R., and De Batist, M., 2016, Late Quaternary evolution of Lago Castor (Chile, 45.6°S): Timing of the deglaciation in northern Patagonia and evolution of the southern westerlies during the last 17 kyr:

- Quaternary Science Reviews, v. 133, p. 130-146,
<https://doi.org/10.1016/j.quascirev.2015.12.021>.
- Vlassenbroeck, J., Dierick, M., Masschaele, B., Cnudde, V., Van Hoorebeke, L., and Jacobs, P., 2007, Software tools for quantification of X-ray microtomography at the UGCT: Nuclear Instruments and Methods in Physics Research Section A: Accelerators, Spectrometers, Detectors and Associated Equipment, v. 580, p. 442-445, <https://doi.org/10.1016/j.nima.2007.05.073>.
- Wang, L., Pan, Y., Li, J., and Qin, H., 2008, Magnetic properties related to thermal treatment of pyrite: Science in China Series D: Earth Sciences, v. 51, p. 1144-1153, <https://doi.org/10.1007/s11430-008-0083-7>.
- Wils, K., Daryono, M. R., Praet, N., Santoso, A. B., Dianto, A., Schmidt, S., Vervoort, M., Huang, J. S., Kusmanto, E., Suandhi, P. A., Natawidjaja, D. H., and De Batist, M., 2021, The sediments of Lake Singkarak and Lake Maninjau in West Sumatra reveal their earthquake, volcanic and rainfall history: Sedimentary Geology, v. 416, 105863, <https://doi.org/10.1016/j.sedgeo.2021.105863>.

TABLE CAPTIONS

Table S2: Grain-size data (D10, mean and sorting) for the 2007 turbidite in cores SN17-02B, SN17-04A, SN17-06A and SN17-09A from Lake Singkarak, calculated using the GRADISTAT package (Blott and Pye, 2001).

Table S3: Magnetic moments (M_s/M_0) for a sample containing a mixture of sediment from all four considered cores in Lake Singkarak during two successive thermal treatments. Normalization for all magnetic moments is done with respect to the initial point of the first heating (M_0), rather than re-normalizing every cycle.

Table S4: Directions of the characteristic remanent magnetization (ChRM) obtained from cores SN17-02B, SN17-04A, SN17-06A and SN17-09A retrieved in Lake Singkarak. The declination and inclination values are calculated by principal component analysis, with indication of the maximum angular deviation (MAD). The underlined values represent unreliable measures of the geomagnetic field, discarded in the

calculation of the average declination values that indicate the north direction in the ChRM reference frame of the U-channel.

Table S5: Orientation data for all digital grains in the 2007 turbidite in Lake Singkarak with an equivalent diameter $>100/150 \mu\text{m}$ and elongation <0.2 . Each tab represents a single turbidite pulse and presents the original φ and θ values as well as the calculated plunge and trend. The orientation of the basal plane used for plunge and trend correction is presented in the upper left corner of each tab.

Table S6: Dominant grain orientations (PC1; eigenvalue, trend and plunge) calculated by the Bingham axial distribution algorithm (Fisher et al., 1987) per pulse and per core (SN17-02B, SN17-04A, SN17-06A and SN17-09A) in Lake Singkarak for all grains presented in Table S5.